

Controlled growth and ordering of poorly-crystalline calcium-silicate-hydrate nanosheets

Felipe Basquiroto de Souza ^{1,3}, Ezzatollah Shamsaei ^{1,3}✉, Shujian Chen ^{1,2}, Kwesi Sagoe-Crentsil ¹ & Wenhui Duan ¹✉

Optimising the mesoscale structure of calcium-silicate-hydrate (C-S-H) is critical to achieving durable and sustainable infrastructure using Portland cement concrete. However, control of its intricate formation process, which comprises spatially disordered growth of poorly-crystalline sheets, remains a challenge. Here, through combination of experimental and computer simulation techniques, we report a promising mechanism to control this complex growth process and thereby optimise the C-S-H nanostructure. The pivotal step was utilizing graphene oxide (GO) to restrain the inherent spatial deformations of the C-S-H sheets and guide their concurrent 2D growth and layer-by-layer ordering. Accordingly, we designed a layered GO-C-S-H composite that exhibits 1–2 orders of magnitude improvement in strength and durability compared with C-S-H formed without control. Our findings open a window for nano-engineering of cements and other complex layered materials for ceramic, pharmaceutical and energy applications.

¹Department of Civil Engineering, Monash University, Clayton, VIC, Australia. ²School of Civil Engineering, The University of Queensland, St Lucia, QLD, Australia. ³These authors contributed equally: Felipe Basquiroto de Souza, Ezzatollah Shamsaei. ✉email: ezzatollah.shamsaei@monash.edu; wenhui.duan@monash.edu

Although calcium–silicate–hydrate ((CaO)_x(SiO₂)_{1-x}_{-y}(H₂O)_y, or C–S–H) governs Portland cement concrete's strength and durability, optimisation of its physico-chemical properties remains a fundamental challenge, restricting improvements in modern infrastructure while contributing to the large carbon footprint of the construction industry (5–10% of global CO₂ emissions)^{1–3}. Despite a century of research^{4–8}, optimisation of C–S–H is hindered by a primary challenge: the difficulty in controlling its mesoscale disorder^{9,10}. When Portland cement is mixed with water, nanometre-thin crumpled sheets/ribbons of C–S–H quickly grow from the cement particles and assemble in a loosely packed, spatially disordered manner^{9,11}. Most of concrete's engineering properties, from its response to mechanical load and chemical attack to time-dependent behaviours such as creep and drying shrinkage, are negatively affected by the loosely packed C–S–H structure^{12–14}. Yet, although vital to enable stronger and more durable cement-based materials^{15,16}, effective mechanisms to control the nucleation/growth and thereby the mesoscale packing of C–S–H are limited.

Hydrothermal treatments can promote the ordered growth of C–S–H (which otherwise take months to years at ambient conditions)^{17,18}, but the need of high temperatures and pressures (>180 °C; ~1 MPa) precludes widespread application. Different starting materials and hydration conditions alter the chemical environment of cements and also affect the nucleation and growth of C–S–H^{9,11}, but due to the chemical complexity of cement systems, establishing the link between chemical composition and the resulting C–S–H mesoscale morphology has proved elusive. Alternatively, adsorbing polymeric dispersants/surfactants onto the C–S–H sheets has been explored to guide their growth and mesoscale packing^{15,16,19}. However, controlling the interplay among the organic molecules, C–S–H sheets, and the highly charged ionic solutions they are embedded in is difficult^{20,21} and only a few successful cases^{15,16} have been reported despite decades of experimental and theoretical research.

Herein, we demonstrate a simple yet effective approach for controlling the complex growth of the C–S–H sheets and, thereby optimise their mesoscale packing to deliver C–S–H-based materials with exceptional properties. Figure 1 summarises our approach. At the mesoscale level, C–S–H is composed of charged, two-dimensional (2D) sheets with a highly defective structure (i.e., poorly crystalline) that approximates that of tobermorite^{22,23}. While the growth of charged particles is usually limited by internal electrostatic repulsion, the extremely high

negative surface charge density of C–S–H and the presence of divalent calcium ions favour the growth of elongated sheets/ribbons (with the relationship between stacking and lateral growth dependent on equilibrium conditions)^{24,25}. On the other hand, the defects in the C–S–H structure cause the sheets to curve (i.e., deform), which hinders their dense stacking and leads to the C–S–H mesoscale disorder (Fig. 1a)^{25–27}.

Following the recent discovery of many geometrically stable 2D materials with unique physicochemical properties²⁸, we used graphene oxide (GO), a 2D material derivative of the graphene family, as confining platforms to counteract the out-of-plane deformations and guide the ordered growth and stacking of C–S–H (Fig. 1b). Via advanced microscopy and spectroscopy, it was found that negatively charged surface of GO strongly interacts with C–S–H via Ca–O bonds (due to the opening of epoxide functional groups) to induce the nucleation and subsequent in-plane growth of the C–S–H sheets. The controlled growth of C–S–H enabled the ordered, layer-by-layer stacking of C–S–H-based composites that, besides outstanding flexibility, possesses tensile strength (>70 MPa), cracking strain (strain capacity >3%) and chemical resistance 1–2 orders of magnitude higher than C–S–H formed without control. Using molecular and structural simulations, we proposed that the observed controlled C–S–H growth arises primarily from a flexural strengthening effect of GO, which counteracts the crystal deformation of defective C–S–H layers and preserves their 2D geometry. These findings unveil new aspirations for cement composites with GO^{29,30} or other 2D materials³¹, and inspire control of related layered materials with analogous molecular-scale ripple deformations^{32,33}.

Results and discussion

Controlled 2D growth. Although other 2D materials could have been used to guide the 2D growth of the C–S–H sheets, we selected GO to use our experiments for several reasons. First, monolayer GO can be reproducibly obtained in large quantities compared with other 2D materials³¹. GO is atomically thin (0.7 nm), atomically flat, and exhibits excellent strength and Young's modulus³⁴, providing a stiff 2D surface to guide the C–S–H growth with minimum material consumption. Most importantly, the surface of GO has abundant oxygen functional groups, which are predicted to, first, act as nucleation sites for the formation of C–S–H³⁵ and, second, coordinate with calcium ions and strongly bond to the C–S–H sheets³⁶.

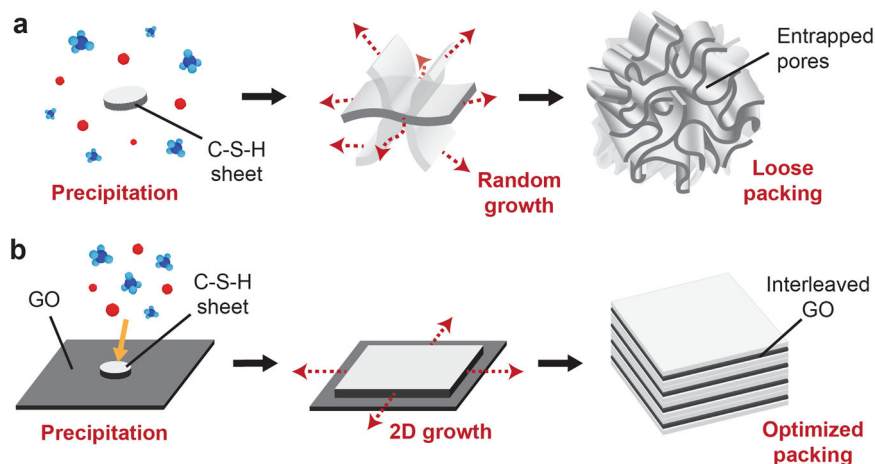


Fig. 1 Approach to controlling the nucleation, growth and packing of C–S–H sheets. **a** Schematic showing the nucleation, growth and loose packing of C–S–H sheets without control. **b** Schematic showing the approach for controlling the nucleation and growth of C–S–H sheets with GO and thereby optimising their nanoscale packing.

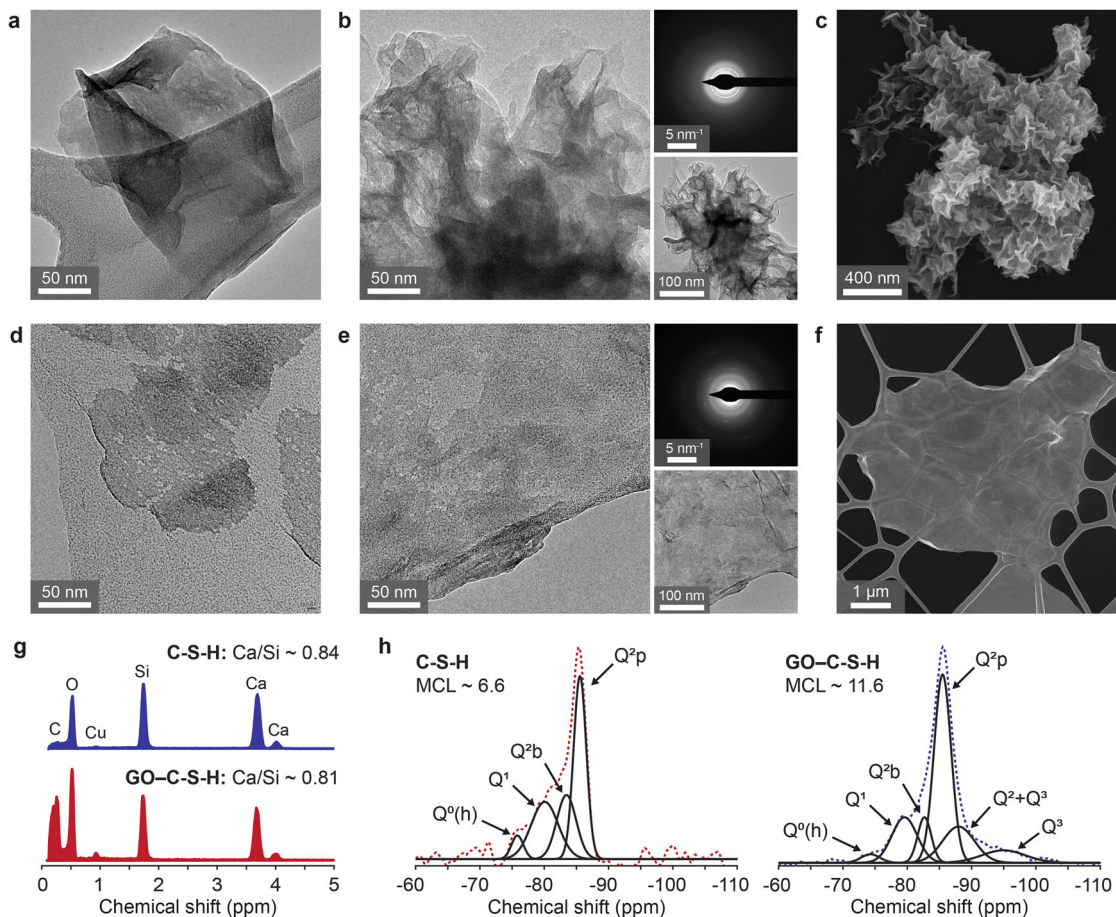


Fig. 2 Control of the growth of C-S-H sheets with GO. **a** TEM image of the folding deformations of a C-S-H sheet without a GO platform. **b, c** Loose packing of C-S-H sheets shown in **b** TEM and **c** SEM images. The top-right and bottom-right images in **(b)** show the selected area electron diffraction and lower-magnification image of the same area, respectively. **d** TEM image showing the 2D geometry of a C-S-H sheet on the surface of GO. Defects (i.e. holes) are seen in the C-S-H sheet. **e** TEM image showing the in-plane C-S-H layer formed on the surface of GO. The top-right and bottom-right images in **(e)** show the selected area electron diffraction pattern and the lower-magnification image of the same area, respectively. **f** SEM image demonstrating the 2D morphology of a single GO-C-S-H mesosheet. **g** EDS analysis of the C-S-H sheets and GO-C-S-H mesosheets. **h** ²⁹Si MAS NMR spectra and MCL of C-S-H formed without and with the GO platforms.

To experimentally realise controlled growth of the C-S-H sheets, C-S-H with Ca:Si ratio of 0.5–1.5 was synthesised in solutions containing highly oxidised, ‘strengthening’ GO sheets (Fig. 2) (for characterisation of GO, see Supplementary Note 1 and Supplementary Fig. 1). This Ca:Si ratio range was selected as it gives rise to C-S-H (I), C-S-H phase prevalent in modern blended cements with siliceous mineral admixtures⁹ and that has been widely used to investigate the fundamental properties of C-S-H³⁷. Figure 2a–c presents the scanning electron microscopy (SEM) and transmission electron microscopy (TEM) images of C-S-H (synthesised with Ca:Si ratio of 1) formed without GO. Without the GO platform, the defective C-S-H sheets show out-of-plane deformations (Fig. 2a). As a result, their assembly is disordered, which results in the commonly observed loose, crumpled mesoscale packing of C-S-H (Fig. 2b, c and Supplementary Fig. 2).

In contrast, Fig. 2d is a TEM image of a C-S-H sheet (synthesised with the same Ca:Si ratio of 1) formed on the GO surface. Although defects (e.g. holes) can be seen, the 2D geometry of the C-S-H sheet is still maintained without out-of-plane deformations, indicating the nanoscale strengthening from GO. As more C-S-H sheets form, the GO surface is covered with a dense, in-plane C-S-H layer (Fig. 2e). Scanning TEM observations in Supplementary Fig. 2 further corroborate that

GO actively guided the 2D growth of the C-S-H sheets. The diffuse ring with a d-spacing range of 0.28–0.33 nm in the selected area electron diffraction (SAED) image (Fig. 2e), in addition to X-ray powder diffraction analysis (Supplementary Fig. 3), confirms that the 2D C-S-H layer is C-S-H (I)^{38,39}. The diffraction results are also similar to that for C-S-H without GO (Fig. 2b and Supplementary Fig. 3). In addition, the scattering of six spots (d-spacing of 0.213 nm) from the monolayer GO was also observed in the SAED image. The SEM image in Fig. 2f shows the micron-scale, 2D morphology of a GO-strengthened C-S-H (referred to as GO-C-S-H) mesosheet, which makes it an ideal building-block for close-packing of C-S-H.

Energy dispersive X-ray spectroscopy (EDS) analysis (Fig. 2g) indicate that the chemical composition of C-S-H is not significantly altered by the GO sheets. On the other hand, ²⁹Si magic-angle spinning (MAS) NMR (Fig. 2h) indicates that the C-S-H in the GO-C-S-H mesosheets possesses a higher degree of polymerisation⁸, with a silicate mean chain length (MCL), nominally, ~76% longer compared with the C-S-H sheets formed without GO (11.6 vs 6.6 tetrahedral units) (for the integral intensity of each silicate group population, see Supplementary Table 1). The higher polymerization degree of the GO-C-S-H mesosheets is further corroborated by Fourier-transform infrared spectroscopy (Supplementary Fig. 3) (Supplementary Note 2

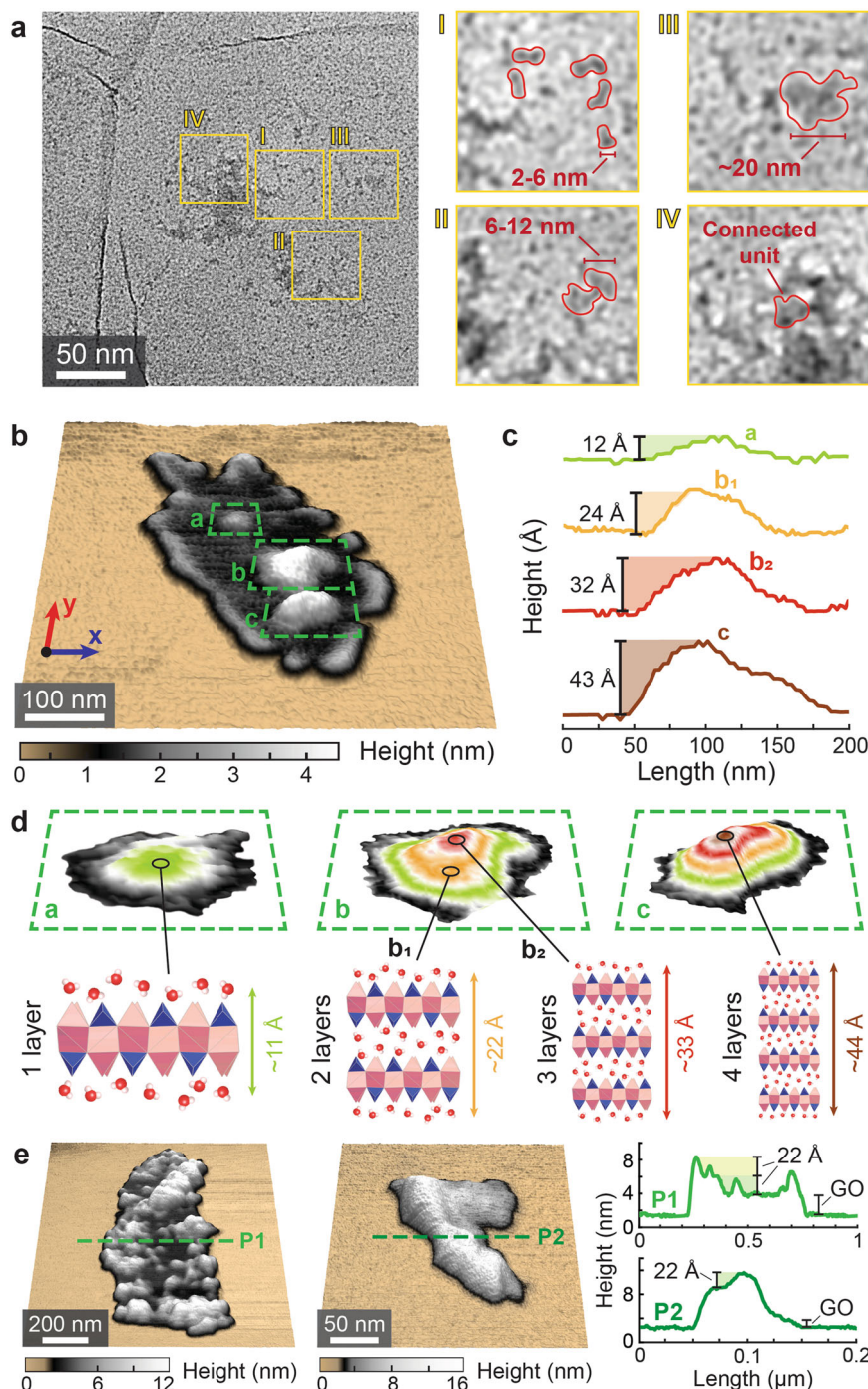


Fig. 3 Nucleation and stacking of single-layer C-S-H sheets on the surface of GO, as observed via TEM and AFM. **a** TEM image of the nucleation of C-S-H precipitates with a lateral size of 2–20 nm on the GO surface. The enlarged images in the regions I–IV were denoised using Gaussian filtering. **b** AFM image of C-S-H precipitates (in white) on the surface of a GO sheet (in black). Three areas ('a', 'b' and 'c') containing C-S-H precipitates are delineated. The GO sheet is sitting on top of a mica substrate (in brown). **c** Height profile passing through the peak of the C-S-H precipitates in the areas 'a', 'b' and 'c'. The precipitate in 'b' has two distinct peaks, denoted as 'b₁' and 'b₂'. **d** The topography level of the C-S-H precipitates suggests regular stacking of 11-Å tobermorite single layers. The topographic contour interval is 1.1 nm. **e** AFM images and height profiles of a GO sheet with several C-S-H precipitates and a GO sheet covered by the in-plane C-S-H layer (GO-C-S-H nanosheet).

describes the supplementary characterisation of C-S-H and the GO-C-S-H mesosheets).

Further insight into the controlled 2D growth of C-S-H was sought by probing the C-S-H precipitates that formed on the GO surface. The TEM image in Fig. 3a shows that GO initially promoted nucleation of very small C-S-H precipitates (region I), with a lateral size as small as 2 nm. Larger C-S-H precipitates

with a size of 10–20 nm were also detected (regions II and III). The uniform electron intensity transmitted through the precipitates suggested their thickness was mostly constant with a sheet-like geometry, confirming that GO prevented nanoscale deformations of the C-S-H sheets from their earliest stage of formation. Moreover, a few of these C-S-H precipitates were interconnected (region IV), demonstrating that the in-plane

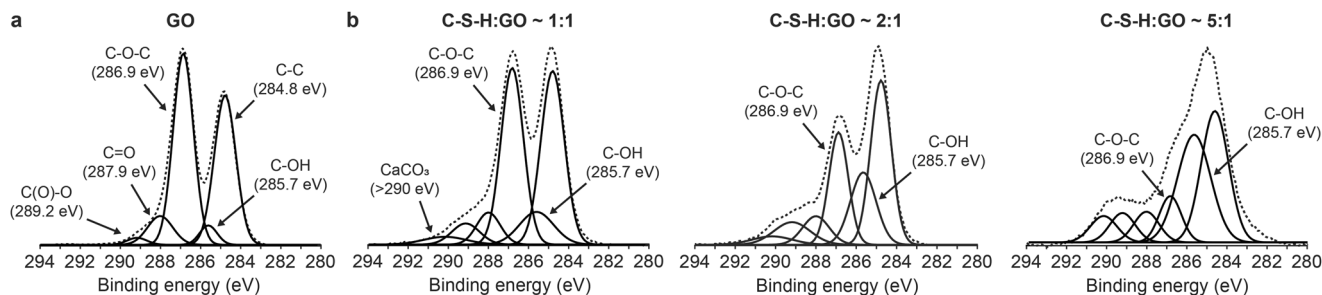


Fig. 4 XPS analysis unveiled the bonding nature between GO and C-S-H on GO-C-S-H mesosheets. **a, b** C 1s XPS spectra of **(a)** GO and **(b)** GO-C-S-H mesosheets with different C-S-H:GO mass ratios indicating the chemical states of carbon in GO before and after the precipitation of C-S-H.

C-S-H layer on GO (Fig. 2e) formed via aggregation of the C-S-H sheets.

In addition to TEM imaging analyses, the thickness of the C-S-H precipitates on a GO sheet was probed via atomic force microscopy (AFM). According to the height profiles shown in Fig. 3b–d, the thinnest C-S-H precipitate (in region ‘a’) had a thickness of 1.18 ± 0.15 nm, which is equivalent to a single layer of 11-Å tobermorite, the crystal analogue of C-S-H (I)³⁷. That is direct evidence that GO controls the geometric deformation of single C-S-H sheets, as further explored in the modelling section. Thicknesses of 2.19 ± 0.27 nm and 3.21 ± 0.15 nm for the precipitate in region ‘b’ and 4.27 ± 0.16 nm in region ‘c’ indicate that the 1.1-nm thick layers can stack regularly onto each other. This regular stacking was also observed in several other C-S-H precipitates and endows the GO-C-S-H mesosheets with their 2D morphology (Fig. 3e).

X-ray photoelectron spectroscopy (XPS) analysis of GO with increasing coverage of C-S-H (i.e., increasing C-S-H:GO mass ratio) suggests that the nucleation and ordered 2D growth of C-S-H is enabled by strong atomic interactions with the GO platform (Fig. 4). As indicated in Fig. 4a, the GO sheets are comprised of carbon atoms bonded via C-C/C=C in aromatic rings (284.6 eV) and oxygen functional groups, mostly epoxy/ether groups (C-O at 286.7 eV) with a minor presence of hydroxyls (C-OH at 285.6 eV), carbonyls (C=O at 288.2 eV), and carboxyls (C(O)-O at 289.4 eV)⁴⁰. On the other hand, as C-S-H precipitates on the surface of GO, the epoxy/alkoxy groups are progressively replaced by hydroxyls (Fig. 4b). This finding is similar to that observed in GO-based materials exposed to divalent ions (e.g. Mg^{2+} and Ca^{2+}). It thus indicates that Ca^{2+} ions, which neutralise the high negative charge density of C-S-H, are attracted to and chemically react with the negatively charged GO surface via ring-opening of epoxide/alkoxy groups⁴⁰. Our XPS results also agree with recent molecular simulations of GO-C-S-H interfaces, which suggest that the Ca^{2+} ions mediate the bonding between the oxygen groups in GO and C-S-H sheets⁴¹. According to ab initio simulations, the bonding is energetically stable and involve the sharing of electrons, indicating its ionic-covalent nature⁴². Interestingly, the epoxide ring-opening reaction is more pronounced in our experiments compared with the simulations (where <10% of the epoxide groups were opened)³⁶. Considering the higher negativity of hydroxyl oxygens compared with epoxide oxygens, these findings indicate that the bonding between GO and C-S-H could be stronger than previously predicted.

The elegance of the GO-guided growth of C-S-H is that it does not depend on precise chemical conditions (e.g., Ca:Si ratio, ionic concentration) as demonstrated in Supplementary Fig. 4 (for experimental details, see Supplementary Note 3 and Supplementary Table 2). This finding is particularly important because cement systems are composed of C-S-H sheets with variations in

chemical composition, formed in solutions with variable ionic concentrations. Nevertheless, for the success of the approach, a few conditions need to be met (Supplementary Fig. 5). First, when the GO sheets were reduced (i.e. oxide groups were removed), they could not prevent deformation of the C-S-H sheets, underpinning the importance of GO-C-S-H interlayer bonding. Second, controlling the precipitation rate of C-S-H is crucial to prevent the formation of C-S-H nuclei in solution¹⁷ rather than in contact with the GO platform. Finally, optimising the ratio between GO and C-S-H is required to achieve control of the C-S-H sheets. After the in-plane C-S-H layer covers the GO surface, subsequent growth of C-S-H sheets was found to be increasingly disordered.

In addition to enabling the controlled growth of synthetic C-S-H, our preliminary results indicate that GO can also guide the growth of C-S-H formed from the dissolution of tricalcium silicate (C3S) cement, the main reactive compound of Portland cement (Supplementary Note 4 and Supplementary Fig. 6)—which demonstrates the potential translation of the approach to nano-engineering bulk cement materials. Due to its chemical robustness, the GO-based approach may also enable nanoscale control of other complex sheet-like materials^{28,32}, such as phyllosilicate materials used for ceramic, polymer, pharmaceutical and energy applications³³. Similar to C-S-H, geometric instabilities also lead to deformations of the sheets and disordered packing of these materials. Nevertheless, further research is needed to confirm this hypothesis as the surface charge properties of these materials can be quite different compared with that of C-S-H, which would influence the pair interaction and bonding with the GO sheets.

Layer-by-layer assembly. To demonstrate the potential of our approach to improving C-S-H-based cements, we assembled the GO-C-S-H mesosheets over an area of several centimetres and nano-engineered a GO-C-S-H-based composite prototype with ultra-high mechanical and durability properties (Fig. 5). Unless otherwise stated, the nano-engineered GO-C-S-H composites possessed Ca:Si ratio of ~ 0.83 and C-S-H:GO mass ratio of ~ 2 (Supplementary Fig. 7) (Supplementary Note 5 describes the supplementary characterisation of the GO-C-S-H composite).

Compared with the loosely packed C-S-H in Fig. 2a–c, the nano-engineered GO-C-S-H has a completely transformed nanostructure. It exhibits highly compact, layer-by-layer packing (Fig. 5a), with the thickness of each layer in the order of 10–15 nm (Fig. 5b), which is the thickness of an individual GO-C-S-H mesosheet (Fig. 3e). The dense packing was corroborated by TEM and nitrogen sorption analysis. Figure 5c shows a TEM image taken from the top of the layered GO-C-S-H. In contrast to the loosely packed C-S-H (Fig. 2b), the transmitted electron intensity is uniform across the layered GO-C-S-H, which demonstrates

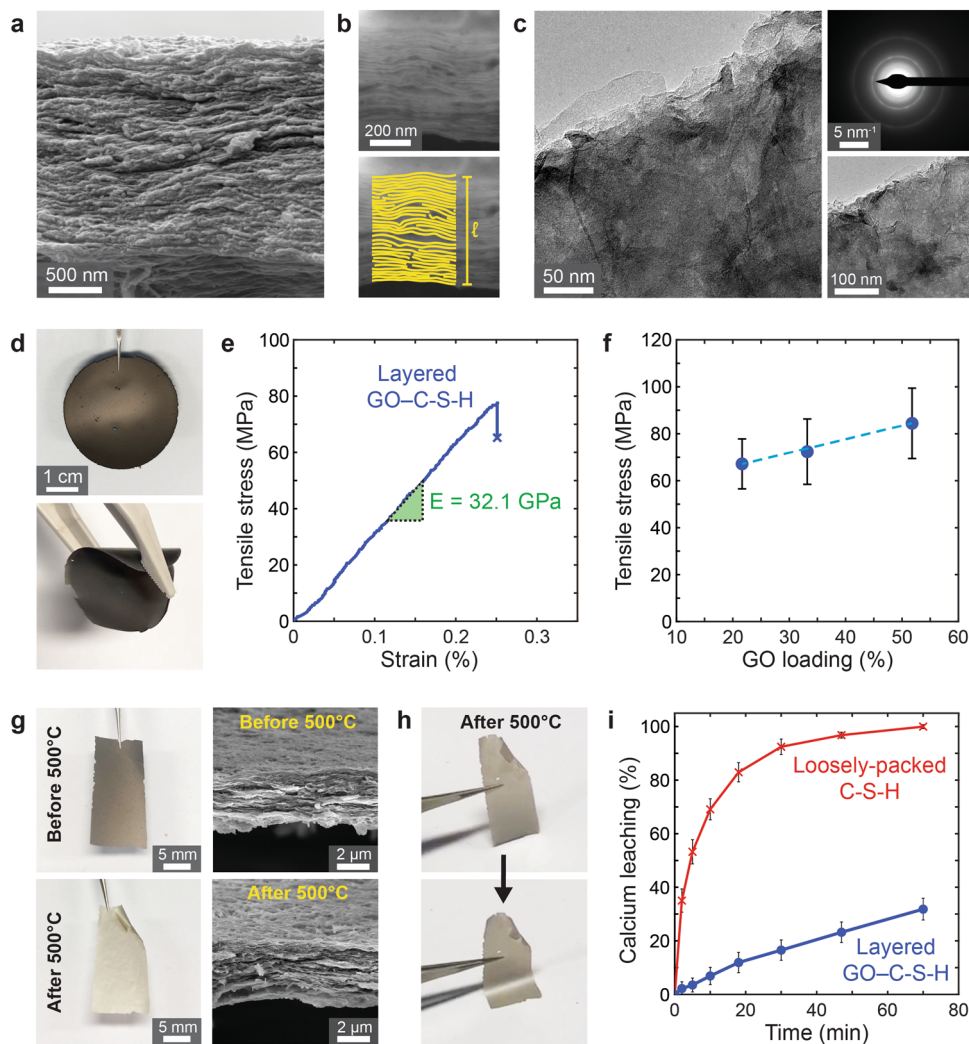


Fig. 5 Nano-engineered layer-by-layer GO-C-S-H with superior mechanical, anti-cracking and chemical properties. **a** SEM images of the cross-section of the layered GO-C-S-H with C-S-H:GO mass ratio of ~2. **b** Cross-section of the layered GO-C-S-H fabricated using a focused-ion-beam instrument. The bottom panel shows the same image as the top panel. Representative lines indicate the layer-by-layer arrangement of the GO-C-S-H nanosheets. The average thickness of a single layer (~10–15 nm) was calculated by dividing the number of layers by the composite total thickness. **c** TEM image of the layered GO-C-S-H. The top-right and bottom-right images in **(c)** show the selected area electron diffraction and the lower-magnification image of the same area, respectively. **d** Digital camera photograph showing the flexibility of the layered GO-C-S-H composite. **e** Tensile stress-strain curve of the layered GO-C-S-H composite. **f** Tensile strength of layered GO-C-S-H composites with different GO loading ratios. Error bars represent the standard deviation of quadruplicate experiments. **g** Digital camera and SEM images showing the layered GO-C-S-H composite before and after exposure to 500 °C for 1 h. **h** Digital camera photographs showing the flexibility of the layered GO-C-S-H composite after exposure to 500 °C for 1 h. **i** Percentage of calcium ions leached from the layered GO-C-S-H structure into ultrapure water over time, compared with loosely packed C-S-H (without control). Error bars represent the standard deviation of duplicate experiments.

the GO-C-S-H mesosheets pack effectively with fewer entrapped pores. The nitrogen sorption measurements (Supplementary Fig. 8) showed that the layered GO-C-S-H had ~40% lower specific surface area and ~70% lower gel pore volume compared with the loosely packed C-S-H.

By manipulating the layered GO-C-S-H composites, we observed remarkable mechanical properties. Figure 5d shows the layered GO-C-S-H composite being manipulated by tweezers and demonstrates its high flexibility, withstanding large elastic deformations without breaking. Furthermore, uniaxial in-plane tension tests using a dynamic mechanical analyser (Fig. 5e) revealed that the layered GO-C-S-H composite had a tensile strength of 72.4 (± 13.9) MPa, which outperforms ordinary C-S-H-based materials by a factor of 10–40 and is equivalent to that of macro-defect-free cement (50–70 MPa)⁴³. Such high

mechanical properties are linked to control of C-S-H's porosity (i.e., defects)⁴³ and possibly to the high elastic modulus of GO³⁴.

To examine the role of the GO sheets on the measured high tensile strength of the layered GO-C-S-H, composites with C-S-H:GO mass ratio of ~1 and ~4 (GO loading of ~20 to ~50%) were also tested (for the chemical composition and Ca:Si ratio of the composites, see Supplementary Fig. 7). As shown in Fig. 5f, increasing the GO loading from ~22% to ~52% (136% increase) only slightly increases the strength of the composites (by ~25%). That indicates that the high tensile strength of the layered GO-C-S-H composites stems primarily from the close-packing of the GO-C-S-H mesosheets, rather than solely attributed to the presence and stiffness of GO sheets. According to the structure–property relationship for layered structured materials⁴⁴, the decrease in strength with increasing C-S-H:GO mass ratio is

possibly associated to the lower elastic modulus of C–S–H compared with GO⁴⁵ and the increased thickness of the mesosheets. Layered GO–C–S–H composites with higher C–S–H:GO mass ratios were attempted (C–S–H:GO > 8), but the composite films were too brittle, likely because of the high disorder of the C–S–H sheets (Supplementary Fig. 5).

Exposing the layered GO–C–S–H composite to an extreme temperature (500 °C) revealed exceptional anti-cracking properties (Fig. 5g, h). C–S–H-based materials crack at high temperatures due to the poor resistance to the nanoscale tensile strains induced by drying shrinkage (strain capacity <0.05%)⁴⁶. As shown in Fig. 5g, the layered GO–C–S–H composites did not present cracks at high temperatures despite exhibiting a shrinkage strain of ~3.6%. Also, the layered GO–C–S–H composite retained its ordered structure (Fig. 5g) and still showed high flexibility after the high-temperature exposure (Fig. 5h). The anti-cracking performance may be attributed to not only the dense packing of the C–S–H sheets, but also to a molecular-scale interlocking effect provided by GO. It was recently demonstrated by molecular simulations that when graphene-based sheets are interleaved within C–S–H layers, they can take up tensile stresses/strains and provide an anti-cracking (i.e., bridging) effect via the strong interfacial bonding with C–S–H, friction, and crack surface adhesion⁴⁷. As a result, the fracture toughness of the interleaved C–S–H nanocomposites can be improved by more than one order of magnitude under in-plane tensile straining compared with a reference C–S–H system⁴⁸. These findings suggest that the layer-by-layer design of the GO–C–S–H composite can effectuate the remarkable toughness enhancements predicted by the molecular simulations.

Decalcification of C–S–H plays a key role in many forms of concrete deterioration (e.g. seawater attack, acid attack and carbonation). To examine its decalcification resistance, we placed the layered GO–C–S–H in a stirred batch reactor⁴⁹ with ultrapure water and measured the amount of calcium leached over time. Leaching of loosely packed C–S–H was also measured under the same conditions. As shown in Fig. 5i, whereas the loosely packed C–S–H rapidly decalcified within few minutes, the layered structure could retain the calcium for considerably longer. According to integral method analysis (Supplementary Fig. 9)⁴⁹, the decalcification rate of the layered GO–C–S–H was 40-fold slower than that of the loosely packed counterpart. These findings demonstrated that controlling the nanoscale packing of C–S–H sheets, and consequently reducing the number of pore channels for chemical attack, can improve the chemical resilience of C–S–H by orders of magnitude. In addition, the higher connectivity of the GO/C–S–H mesosheets (Fig. 2h) may have helped improving the composite chemical stability as well.

Nano-strengthening mechanism. We propose a nanomechanical mechanism to explain how GO enables the ordered 2D growth of C–S–H. While there are two main views of the C–S–H nanostructure, namely the granular and continuous models²⁷, the latter is followed here. According to Gartner's sheet growth model²⁶, defects in the atomic structure induce the folding deformation of single-layer sheets of C–S–H (Fig. 6a) and lead to the spatially disordered growth process^{25,27}. By examining the problem from a nanomechanical perspective, we hypothesised that the mechanically strong GO sheets can control the molecular-scale instabilities of the C–S–H single-layer sheets (as observed in Fig. 3c) by functioning as nano-strengthening materials (Fig. 6b). Analogous to the strengthening of load-bearing structures (e.g., flexural strengthening of slabs with carbon textile or steel plates)⁵⁰, the strengthening should increase the flexural moment capacity of the

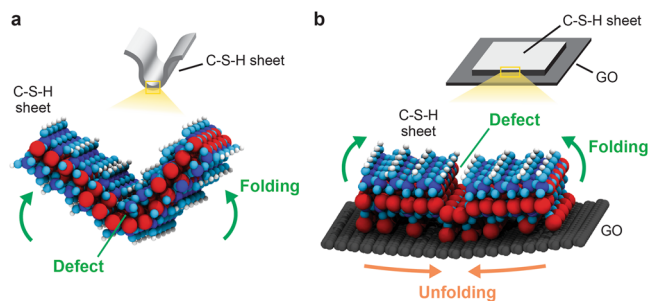


Fig. 6 Proposed nanomechanical mechanism for the controlled growth of C–S–H sheets with GO. **a** According to the C–S–H sheet growth model²⁶, crystal instabilities (i.e. defects) induce the geometric deformation of the C–S–H sheets, which leads to their spatially disordered growth. **b** Schematic showing the proposed nanomechanical mechanism for the GO-enabled control of the C–S–H growth. GO functions as a nano-strengthening material to counteract the C–S–H sheets' nanoscale deformations and preserve their in-plane geometry, enabling the 2D ordered growth. Red, light-blue, dark-blue, white and dark-grey circles indicate the Ca, O, Si, H, and C atoms, respectively.

C–S–H sheets and thereby increase the energy required to induce their folding deformations.

To validate this hypothesis, a series of molecular mechanics (MM) molecular dynamics (MD), density functional theory (DFT) and finite element method (FEM) calculations were performed in two main stages. First, we built a comprehensive molecular model using MD and DFT to understand the dynamics and energetics associated with the deformation of defective C–S–H sheets. Second, FEM structural analysis was used to demonstrate the role of GO in mechanically hindering the C–S–H deformations.

Following recently proposed C–S–H models^{22,23,51,52}, C–S–H with realistic atomic structures were constructed by inserting crystal defects into the known structure 11-Å tobermorite, the crystal analogue of C–S–H (I)³⁷ (for the model construction procedure, see Supplementary Note 6 and Supplementary Fig. 10). Although far from perfect, we adopted models based on the so-called defective tobermorite because they have been demonstrated to adequately reproduce the physicochemical properties of C–S–H^{22,23}. In a nutshell, we first built a supercell of 11 Å tobermorite ($1 \times 3 \times 0.5$ in an armchair direction or $3 \times 1 \times 0.5$ in a zig-zag direction) to represent a small section of a C–S–H sheet. The interlayer calcium ions and silicate bridging tetrahedra were removed, giving a Ca:Si ratio of 1, the same ratio used in most of our experiments. As proposed by Gartner and other C–S–H models^{22,26}, defects were then created by removing one silicate dimer from the C–S–H structure (i.e., creating a hinge) (Fig. 7a). Finally, the defective C–S–H structures were placed in a periodic simulation box (see 'Methods') filled with water molecules.

To analyse the geometric stability of the defective C–S–H structures, a 50-ps simulated annealing of 12 configurations hinged in both the armchair and zig-zag crystal direction was performed via MM/MD simulations (Supplementary Fig. 11). Out of the 12 structures, three configurations in the zig-zag direction and one in the armchair direction displayed significant deformations (Supplementary Fig. 12), confirming previous predictions²⁶ that missing silicate dimers can lead to the formation of stable folded structures. Using DFT, the folding process energetics was then examined by optimising and computing the energy of the C–S–H structures obtained before and after folding. For this step, explicit water molecules covering the C–S–H surface and an implicit solvation shell⁵³ were considered (Fig. 7b). We found that C–S–H sheets hinged in

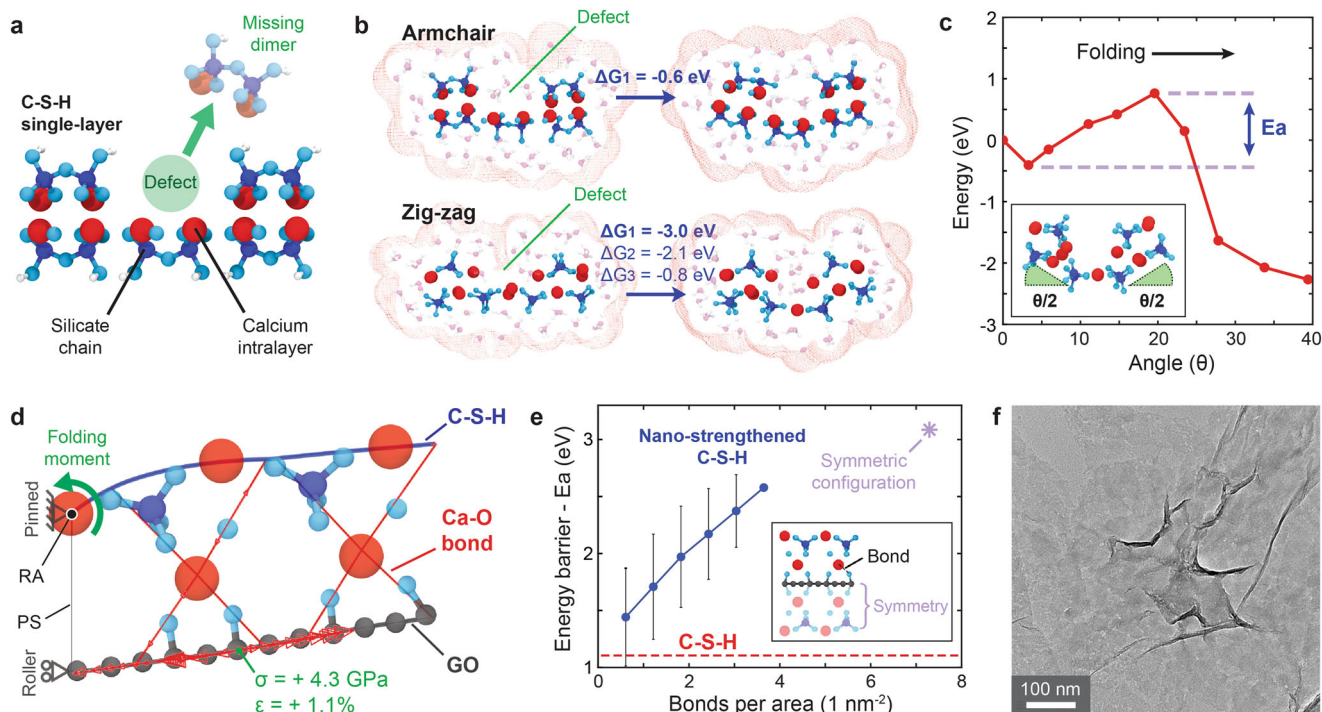


Fig. 7 Theoretical validation of the GO-strengthening mechanism for controlling the inherent spatial deformations of C-S-H sheets. **a** Atomic structure of a defective C-S-H single layer with a missing silicate dimer. **b** Free energy difference (ΔG) of the hinged C-S-H sheets before and after folding conformations, as calculated by DFT. **c** Energy path for C-S-H folding conformation with the highest ΔG , as calculated by the nudged elastic band method. The energy barrier (E_a) is indicated. Inset: folding angle θ is defined as the tilt displacement of the CaO layer (see Supplementary Fig. 12). **d** Snapshot of the FEM simulations showing the stress and strain in a GO-strengthened C-S-H layer as is deformed. C-S-H and GO are represented by two parallel beams connected via cross-bracing elements representing the Ca-O bonds. The model has symmetrical boundary conditions. RA rotation axis, PS plane of symmetry. **e** Energy barrier required to fold GO-strengthened C-S-H, as a function of the number of bonds per area. The energy barrier value (-1.17 eV) of the C-S-H without strengthening is marked with a dashed line. Inset: bonding between C-S-H and GO and the symmetrical configuration considered in the calculations. Error bars represent the standard deviation of at least six different configurations (see Supplementary Fig. 15). Red, light-blue, dark-blue, white and dark-grey circles indicate the Ca, O, Si, H and C atoms, respectively. **f** TEM image showing the folding deformations of a C-S-H sheet on the surface of reduced GO.

the zig-zag direction were less energetically stable compared with the armchair direction, presenting higher free energy differences (ΔG) between unfolded and folded structures (Fig. 7b). This finding is consistent with previous simulations of tobermorite nanotubes⁵⁴, which suggests that C-S-H structures are more stable along the silicate chain backbone (i.e. armchair). Further insight about the C-S-H folding process was obtained via DFT/nudged elastic band method⁵⁵. To compute the folding energy path, the unfolded and folded states of the zig-zag structure with the highest ΔG (-3.04 eV), corresponding to the highest associated folding moment (Supplementary Table 3), were used as the start and end coordinates. The results shown in Fig. 7c revealed that, because of the rearrangement of chemically bound water molecules, the defective C-S-H sheet needs to overcome an energy barrier (E_a) before folding, indicating that the deformation process is kinetically controlled.

We therefore hypothesised that the combination of C-S-H sheets with GO (Fig. 6b) would counteract the C-S-H folding by increasing this activation energy and thereby slowing the deformation process. FEM nonlinear static calculations validated our hypothesis. C-S-H sheets strengthened by monolayer GO were modelled as 2D-braced frames, where C-S-H and GO are represented by two parallel beam elements connected via cross-bracing truss elements representing the Ca-O bonds (Fig. 7d) (for model considerations, see Supplementary Note 7 and Supplementary Fig. 13). The cross-braced adopted in our model assumes that each Ca ion coordinates with two nonbridging tetrahedra

from C-S-H and two hydroxyl groups from GO, which is consistent with our experimental observations in Fig. 4 and previous reactive molecular simulations³⁶. The employed symmetric boundary conditions and properties of the elements are summarised in Fig. 7d and Supplementary Table 4, respectively. Folding of the GO-C-S-H structures was induced by applying a linearly increased point moment at a selected axis of rotation, which represented the hinge defect. The energy required to tilt the GO-C-S-H structures was obtained by calculating the involved mechanical work, defined as the product of the point moment and folding angle (Supplementary Fig. 14).

As shown in Fig. 7d, when a point moment induced the folding of the GO-C-S-H structure, GO was subjected to tensile strains that generated an opposite moment counteracting the deformation. Because of GO's high in-plane stiffness, this strengthening effect increased the activation energy needed to fold C-S-H from 1.17 to 2.58 eV (Supplementary Fig. 14). According to the Arrhenius equation (see 'Methods'), such an increase in the energy barrier can decrease the likelihood of folding by up to 23 orders of magnitude, confirming that the GO support can make the C-S-H folding kinetically inaccessible during the crystal growth phase. Taking into consideration the growth of C-S-H on both sides of GO or possible instability of GO's functional groups³⁶, we respectively simulated the folding of a symmetric GO-C-S-H structure and structures with different bonding configurations (Supplementary Fig. 15). Figure 7e shows that, in the case of a symmetrical configuration, the energy barrier to

activating C–S–H folding can be further increased to 3.09 eV. On the other hand, we found that the increase in energy barrier is linearly dependent on the number of bonds between the C–S–H and GO sheets. This finding reiterates the importance of the interlayer bonding between GO and C–S–H—consistent with the experimental observations, which demonstrated the failure of the nano-strengthening when reduced GO sheets were used as platforms (Fig. 7f and Supplementary Fig. 5). Other parameters such as pH, which can affect the degree of protonation and stability of GO's functional groups, are thus predicted to also play a role in successfully controlling the growth of C–S–H.

Conclusion

Through experimental and theoretical investigation, we unveiled an approach of controlling the nucleation, growth and packing of poorly crystalline nanometre-thin sheets to thereby transform the properties of C–S–H. We first experimentally demonstrated that GO sheets are excellent platforms to restrain the inherent spatial deformation of C–S–H sheets and guide their ordered 2D growth. With the successful control over their geometry, we assembled the C–S–H sheets in a layer-by-layer manner and obtained GO–C–S–H composites with high flexibility, tensile strength (>70 MPa), cracking strain (strain capacity >3%) and chemical resistance, delivering overall performance unmatched by any known C–S–H-based material. Finally, we theoretically validated that GO functions as a nano-strengthening material to increase the bending capacity of individual C–S–H sheets and thereby preserve their 2D geometry.

The bottom-up design and remarkable properties of the nano-engineered C–S–H material raise prospects for a generation of remarkably high-performance cementitious materials. Recently, mixing GO and other 2D materials into bulk cementitious materials has attracted great interest^{29,31} but in those cases, C–S–H was still largely disordered and the reported composites showed limited improvement in tensile strength (<10 MPa) and durability³⁰. We have demonstrated here how breakthroughs in the properties of cement composites with GO can be achieved by exploiting their nanomechanical properties and controlling the packing of C–S–H sheets. We anticipate that further improvements of nano-engineered C–S–H-based materials can be achieved by exploring different interatomic interactions between the C–S–H sheets, 2D materials and additional phases such as polymers and nanofibres. For example, graphene-based composites that are stronger than steel have been fabricated by carefully controlling these interactions⁵⁶. From the macroscale perspective, the process of scaling up the layered GO–C–S–H phases into bulk cementitious materials might be similar to that currently employed in vacuum dewatering, spraying, and mechanical pressing methods (such as those used for fabricating macro-defect-free cement⁴³). The realisation of such materials can potentially enable the smart design of concrete with ultra-high strength and durability, leading to cost-effective and highly durable infrastructure with a reduced carbon footprint.

Methods

Synthesis of C–S–H and GO–C–S–H. C–S–H was synthesised via double decomposition of calcium nitrate and sodium silicate¹⁷. In a typical synthetic procedure, 9 mL of Ca(NO₃)₂·4H₂O (4.72 mg mL⁻¹) was injected dropwise at an addition rate of 0.15 mL min⁻¹ into a magnetically stirred mixture of 9 mL of Na₂SiO₃ (2.44 mg mL⁻¹) and 5 mL of ultrapure water to form C–S–H (with an initial Ca:Si molar ratio of 1). To form the GO–C–S–H mesosheets (with an initial stoichiometric C–S–H:GO mass ratio of 2.4), the 5 mL of ultrapure water contained GO at a concentration of 2 mg mL⁻¹. The Ca:Si and C–S–H:GO ratios of the GO–C–S–H mesosheets were modified by varying the initial concentration of the Ca(NO₃)₂·4H₂O and Na₂SiO₃ precursors or of the GO dispersions. The pH of the solution was adjusted to ~13.0 by adding NaOH (2.5 M) into the Na₂SiO₃ solution. The dispersions were aged for 2 h under stirring. To stop the C–S–H reaction and remove the Na⁺ and NO₃⁻ salts, the solutions were washed once in deionised water

and then washed several times in ethanol. Experiments were performed at room temperature. Freshly boiled CO₂-free deionised water was used and all the described steps were performed in an N₂ environment.

Layered GO–C–S–H. Large-sized layered GO–C–S–H composite materials were prepared by precipitating the GO–C–S–H mesosheets from solution via vacuum filtration. A 300-mL ethanol dispersion of GO–C–S–H nanosheets (~6 μg mL⁻¹) was vacuum filtered through an Anodisc membrane filter (47 mm in diameter, 0.1 μm pore size), followed by vacuum drying and peeling from the filter. Layered GO–C–S–H composites of ~2–3 μm thickness were fabricated by adjusting the concentration of the GO–C–S–H mesosheets dispersion. The Ca:Si and C–S–H:GO ratios of the composites were confirmed via XPS elemental analysis (Supplementary Fig. 7). For testing, the layered GO–C–S–H composites were cut by scissors without further modification.

Microscopy. SEM imaging was performed with a FEI Nova NanoSEM 450 FEG-SEM or FEI Magellan 400 XHR FEGSEM instrument operated at 2–5 kV. Cross-sections of the layered GO–C–S–H fabricated by focused ion beam were created and imaged using a FEI Helios NanoLab 600 Dual Beam operated at 5–10 kV. TEM imaging and selected area diffraction were performed using a FEI Tecnai T20 instrument operated at 200 kV. The topography of the GO–C–S–H nanosheets was mapped in a Bruker's Dimension Icon AFM using a doped monolithic silicon-coated tip with a 23-nm thick platinum iridium 5 layer (Arrow™ NCPt). The AFM images were processed using the Gwyddion open-source software.

Spectroscopy. EDS, coupled to the TEM instrument, was obtained using a Bruker 30 mm² ultrathin window silicon drift detector and Quantax analysis system. The small trace of Cu in the EDS spectra derives from the Cu holey carbon grid used to mount the samples. XPS was performed with a ThermoFisher Scientific Nexsa Surface Analysis System using a monochromated Al Kα source. The ²⁹Si MAS NMR spectra were acquired using a Bruker AV 500 M spectrometer. Deconvolution curves were calculated by fitting multiple normal distribution curves to the raw experimental data. The peak values for the silicate species Q⁰, Q¹, Q^{2b}, Q^{2p}, Q²⁺ and Q³ were within the range of 70–76, 78–80, 82–84, 84–86, 88–95 and 95–100 ppm, respectively. These values were determined according to previous studies in cement composites⁸. The MCL of C–S–H was estimated according to the equation:

$$\text{MCL} = \frac{2(Q^1 + Q^2 + Q^3)}{Q^1} \quad (1)$$

Tensile strength. The tensile strength of the layered GO–C–S–H composite was measured by static mechanical uniaxial in-plane tension tests using a dynamic mechanical analyser (Perkin Elmer DMA 8000), following a similar method adopted for testing GO composite materials⁴⁰. The sample length and width between the clamps were measured using standard calipers and the sample thickness was obtained from SEM imaging of the composite cross-section. The layered GO–C–S–H composite was mounted on the tension clamps of the DMA and the tensile tests were carried with a preload of 0.01 N and a force ramp rate of 0.05 N min⁻¹ until the sample ruptured. The mean value and standard deviation were calculated from quadruplicate experiments.

High temperature. As typically applied in the study of cement materials under high temperatures, the cracking resistance of the layered GO–C–S–H composite was evaluated by heating (heating rate of 10 °C min⁻¹) the samples up to 500 °C in a muffle furnace. The samples were maintained at this temperature for 1 h, then removed from the furnace and allowed to cool down to room temperature for 1 h. To calculate the drying shrinkage, the sample length and width before and after heat exposure were measured using standard calipers. Experiments were performed in quadruplicate.

Decalcification. A batch reactor method⁴⁹ was used to measure the decalcification rate constant of the loosely packed and layered GO–C–S–H phases. The loosely packed C–S–H was synthesised with the same Ca:Si ratio (~0.85) as the layered GO–C–S–H and vacuum dried before experiments. For the experiments, a given weight (~3–4 mg) of the solid material was added to a flask containing 100 mL of ultrapure water (pH 5). The flask was capped and magnetically stirred at 100 rpm at ~25 °C. Aliquots were collected at 2, 5, 10, 18, 30, 47 and 70 min, filtered and acidified with hydrochloric acid. The quantity of calcium leached into the solution was determined by inductively coupled plasma–optical emission spectrometry (ICP-OES, Perkin Elmer Optima 7000 DV). After 70 min, the solution was acidified with hydrochloric acid to dissolve the remaining solid material. The solution was then analysed by ICP-OES to determine the calcium content of the solid material before decalcification. The weight of the solid material was controlled so that all samples contained similar calcium content before decalcification (difference within 5%). The decalcification percentage was calculated by dividing the quantity of calcium leached into the solution at a given time by the calcium content of the

solids before decalcification. Mean values and standard deviation error bars were calculated from duplicate experiments.

MD simulations. The folding deformations of defective C–S–H sheets were explored by MD simulations using the open-source simulation code LAMMPS (code freely available at <https://lammps.sandia.gov>). A periodic simulation box ($6.735 \times 50 \times 35 \text{ \AA}$ in the armchair direction and $50 \times 7.425 \times 35 \text{ \AA}$ in the zig-zag direction) packed with water molecules was created to simulate C–S–H structures in an aqueous environment. The MD simulations were carried out by first using a 5-ps-long NVE ensemble to relax the system. Then, the 50-ps-long simulated annealing in a temperature range from 300 to 360 K was performed using an NPT ensemble (1 atm; the box's dimensions were constant in the *a*-axis for the armchair direction and the *b*-axis for the zig-zag direction). Atomic interactions were modelled by ClayFF force field⁵⁷ for two main reasons. First, previous studies confirmed that ClayFF can accurately describe the structural and dynamic properties of hydrated mineral systems and their interfaces with aqueous solutions, including C–S–H systems^{57,58}. Second, given the large scale of the MD simulations (~1000 atoms), ClayFF is more efficient compared with core-shell models⁵⁹. To confirm that the results were not exclusive to the selected force-field potentials, the simulations were also performed with CSH-FF⁵⁹, a re-parameterised version of ClayFF (Supplementary Fig. 12).

DFT. DFT was used to optimise and calculate the free energy of the C–S–H structures obtained by MD simulations. The calculations were completed using the CP2K programme package (code freely available at <https://www.cp2k.org/>). The hybrid Gaussian and plane wave method⁶⁰ with Goedecker–Teter–Hutter pseudopotential parameters optimised for Perdew–Burke–Erzerhof⁶¹ and with a double-zeta valence molecularly optimised (shorter range) basis set⁶² were used. The plane wave density cut-off was 400 Ry, with a relative cut-off of 40 Ry. The energy path of the C–S–H folding deformation was computed using the climbing image nudged elastic band method⁶³ with the spring constant value set to 0.05 au. To accurately represent the C–S–H structures in their saturated state, explicit water molecules (ratio: CaO:SiO₂:4H₂O) and implicit self-consistent continuum solvation⁶⁴ ($\rho_{\text{min}} = 0.00001 \text{ au}$; $\rho_{\text{max}} = 0.0001 \text{ au}$) were considered in the DFT calculations. The C–S–H structures remained stable after the DFT geometry optimisation. Only small changes in bond distances (<1.5%) and the position of water molecules were observed, while the overall geometry of the C–S–H structures was unmodified.

FEM calculations. FEM nonlinear static analysis by Abaqus/CAE software was used to calculate the strengthening effect of GO during C–S–H folding. FEM has been previously used to analyze the mechanical behaviour of nanostructures⁶³ and was chosen for two main reasons. First, this method could determine the energy required to fold the GO–C–S–H structures, which could be directly compared with the MD and DFT results. Second, this approach could elucidate the transfer of stresses between C–S–H and GO via the Ca–O interlayer bonding as folding deformation progresses. The GO–C–S–H composite structure was modelled as a planar frame, with the length of the elements determined according to the bonding distances of GO and 11-Å tobermorite reported in the literature (Supplementary Fig. 13). The Arrhenius equation

$$\frac{k_{\text{CSH}}}{k_{\text{GO/CSH}}} = \frac{E_a}{e^{k_B T}} \quad (2)$$

where E_a is the activation energy, T is the absolute temperature and k_B is the Boltzmann constant, was used to calculate the ratio between the C–S–H and GO–C–S–H folding rate constants (k).

Data availability

All data generated or analysed during this study are included in this published article (and its supplementary information files). Additional data related to this study are available from the corresponding author on reasonable request.

Received: 10 November 2020; Accepted: 21 July 2021;

Published online: 11 August 2021

References

- Monteiro, P. J. M., Miller, S. A. & Horvath, A. Towards sustainable concrete. *Nat. Mater.* **16**, 698–699 (2017).
- Liu, Z. et al. Reduced carbon emission estimates from fossil fuel combustion and cement production in China. *Nature* **524**, 335–338 (2015).
- Habert G. et al. Environmental impacts and decarbonization strategies in the cement and concrete industries. *Nat. Rev. Earth Environ.* **1**, 559–573 (2020).
- Le Chatelier H. *Experimental Researches on the Constitution of Hydraulic Mortars* (McGraw Publishing Company, 1905).
- Chatterji, S. & Jeffery, J. Three-dimensional arrangement of hydration products in set cement paste. *Nature* **209**, 1233–1234 (1966).
- Double, D. & Hellawell, A. The hydration of Portland cement. *Nature* **261**, 486–488 (1976).
- Allen, A. J., Thomas, J. J. & Jennings, H. M. Composition and density of nanoscale calcium–silicate–hydrate in cement. *Nat. Mater.* **6**, 311 (2007).
- Pustovgar, E. et al. Understanding silicate hydration from quantitative analyses of hydrating tricalcium silicates. *Nat. Commun.* **7**, 10952 (2016).
- Richardson, I. Tobermorite/jennite-and tobermorite/calcium hydroxide-based models for the structure of CSH: applicability to hardened pastes of tricalcium silicate, β-dicalcium silicate, Portland cement, and blends of Portland cement with blast-furnace slag, metakaolin, or silica fume. *Cem. Concr. Res.* **34**, 1733–1777 (2004).
- Ioannidou, K. et al. Mesoscale texture of cement hydrates. *Proc. Natl Acad. Sci. USA* **113**, 2029–2034 (2016).
- Zhang, Z., Scherer, G. W. & Bauer, A. Morphology of cementitious material during early hydration. *Cem. Concr. Res.* **107**, 85–100 (2018).
- Morshedifard, A., Masoumi, S. & Qomi, M. A. Nanoscale origins of creep in calcium silicate hydrates. *Nat. Commun.* **9**, 1785 (2018).
- Nguyen, H., Rahimi-Aghdam, S. & Bažant, Z. P. Unsaturated nanoporomechanics. *Proc. Natl Acad. Sci. USA* **117**, 3440–3445 (2020).
- Ioannidou, K. et al. The crucial effect of early-stage gelation on the mechanical properties of cement hydrates. *Nat. Commun.* **7**, 12106 (2016).
- Picker, A. et al. Mesocrystalline calcium silicate hydrate: a bioinspired route toward elastic concrete materials. *Sci. Adv.* **3**, e1701216 (2017).
- Moghaddam, S. E. et al. Morphogenesis of cement hydrate. *J. Mater. Chem. A* **5**, 3798–3811 (2017).
- Wu, J., Zhu, Y. J. & Chen, F. Ultrathin calcium silicate hydrate nanosheets with large specific surface areas: synthesis, crystallization, layered self-assembly and applications as excellent adsorbents for drug, protein, and metal ions. *Small* **9**, 2911–2925 (2013).
- Gmira, A., Zabat, M., Pellenq, R.-M. & Van Damme, H. Microscopic physical basis of the poromechanical behavior of cement-based materials. *Mater. Struct.* **37**, 3–14 (2004).
- Matsuyama, H. & Young, J. F. Intercalation of polymers in calcium silicate hydrate: a new synthetic approach to biocomposites? *Chem. Mater.* **11**, 16–19 (1999).
- Turesson, M., Labbez, C. & Nonat, A. Calcium mediated polyelectrolyte adsorption on like-charged surfaces. *Langmuir* **27**, 13572–13581 (2011).
- Picker, A., Nicoleau, L., Nonat, A., Labbez, C. & Cölfen, H. Identification of binding peptides on calcium silicate hydrate: a novel view on cement additives. *Adv. Mater.* **26**, 1135–1140 (2014).
- Qomi, M. A. et al. Combinatorial molecular optimization of cement hydrates. *Nat. Commun.* **5**, 4960 (2014).
- Pellenq, R. J.-M. et al. A realistic molecular model of cement hydrates. *Proc. Natl Acad. Sci. USA* **106**, 16102–16107 (2009).
- Delhorme, M. et al. Aggregation of calcium silicate hydrate nanoplatelets. *Langmuir* **32**, 2058–2066 (2016).
- Ioannidou, K., Pellenq, R. J.-M. & Del Gado, E. Controlling local packing and growth in calcium–silicate–hydrate gels. *Soft Matter* **10**, 1121–1133 (2014).
- Gartner, E. M. A proposed mechanism for the growth of C • S • H during the hydration of tricalcium silicate. *Cem. Concr. Res.* **27**, 665–672 (1997).
- Nguyen-Tuan, L., Etzold, M. A., Rößler, C. & Ludwig, H.-M. Growth and porosity of CSH phases using the sheet growth model. *Cem. Concr. Res.* **129**, 105960 (2020).
- Novoselov K., Mishchenko A., Carvalho A. & Castro Neto A. H. 2D materials and van der Waals heterostructures. *Science* **353**, acc9439 (2016).
- Luong, D. X. et al. Gram-scale bottom-up flash graphene synthesis. *Nature* **577**, 647–651 (2020).
- Shamsaei, E. et al. Graphene-based nanosheets for stronger and more durable concrete: a review. *Constr. Build. Mater.* **183**, 642–660 (2018).
- Wang, W., Chen, S. J., De Souza, F. B., Wu, B. & Duan, W. H. Exfoliation and dispersion of boron nitride nanosheets to enhance ordinary Portland cement paste. *Nanoscale* **10**, 1004–1014 (2018).
- Kou, L., Ma, Y., Smith, S. C. & Chen, C. Anisotropic ripple deformation in phosphorene. *J. Phys. Chem. Lett.* **6**, 1509–1513 (2015).
- Aslin, J., Mariani, E., Dawson, K. & Barsoum, M. W. Ripplifications provide a new mechanism for the deformation of phyllosilicates in the lithosphere. *Nat. Commun.* **10**, 1–9 (2019).
- Cao, C., Daly, M., Singh, C. V., Sun, Y. & Filleter, T. High strength measurement of monolayer graphene oxide. *Carbon* **81**, 497–504 (2015).
- Du, T., Li, H. & Bauchy, M. Molecular dynamics simulation of the precipitation of calcium silicate hydrate nanostructures under two-dimensional confinement by TiO₂: implications for advanced concretes. *ACS Appl. Nano Mater.* **3**, 2176–2184 (2020).
- Kai, M., Zhang, L. & Liew, K. Graphene and graphene oxide in calcium silicate hydrates: chemical reactions, mechanical behavior and interfacial sliding. *Carbon* **146**, 181–193 (2019).

37. Skinner, L., Chae, S., Benmore, C., Wenk, H. & Monteiro, P. Nanostructure of calcium silicate hydrates in cements. *Phys. Rev. Lett.* **104**, 195502 (2010).
38. Taylor H. F. W. *Cement Chemistry*, 2nd edn (Thomas Telford, 1997).
39. Viehland, D., Li, J. F., Yuan, L. J. & Xu, Z. Mesostructure of calcium silicate hydrate (C-S-H) gels in portland cement paste: short-range ordering, nanocrystallinity, and local compositional order. *J. Am. Ceram. Soc.* **79**, 1731–1744 (1996).
40. Park, S. et al. Graphene oxide papers modified by divalent ions—enhancing mechanical properties via chemical cross-linking. *ACS Nano* **2**, 572–578 (2008).
41. Hou, D., Yang, T., Tang, J. & Li, S. Reactive force-field molecular dynamics study on graphene oxide reinforced cement composite: functional group deprotonation, interfacial bonding and strengthening mechanism. *Phys. Chem. Chem. Phys.* **20**, 8773–8789 (2018).
42. Hosseini, E., Zakertabrizi, M., Korayem, A. H., Chen, S. & Mohsenabadi, S. K. Graphene oxide in ceramic-based layered structure: nanosheet optimization. *Constr. Build. Mater.* **224**, 266–275 (2019).
43. Birchall, J., Howard, A. & Kendall, K. Flexural strength and porosity of cements. *Nature* **289**, 388 (1981).
44. Sakhavand, N. & Shahsavari, R. Universal composition–structure–property maps for natural and biomimetic platelet–matrix composites and stacked heterostructures. *Nat. Commun.* **6**, 1–13 (2015).
45. Hou, D., Zhu, Y., Lu, Y. & Li, Z. Mechanical properties of calcium silicate hydrate (C–S–H) at nano-scale: a molecular dynamics study. *Mater. Chem. Phys.* **146**, 503–511 (2014).
46. Bentz, D. P. & Jensen, O. M. Mitigation strategies for autogenous shrinkage cracking. *Cem. Concr. Compos.* **26**, 677–685 (2004).
47. Chen, S. J., Li, C. Y., Wang, Q. & Duan, W. H. Reinforcing mechanism of graphene at atomic level: Friction, crack surface adhesion and 2D geometry. *Carbon* **114**, 557–565 (2017).
48. Al-Muhit, B. & Sanchez, F. Nano-engineering of the mechanical properties of tobermorite 14 Å with graphene via molecular dynamics simulations. *Constr. Build. Mater.* **233**, 117237 (2020).
49. Brantley S. L., Kubicki J. D. & White A. F. *Kinetics of Water-Rock Interaction* (Springer Science+Business Media, 2008).
50. Spadea, G., Bencardino, F. & Swamy, R. Structural behavior of composite RC beams with externally bonded CFRP. *J. Compos. Constr.* **2**, 132–137 (1998).
51. Kovačević, G., Persson, B., Nicoleau, L., Nonat, A. & Veryazov, V. Atomistic modeling of crystal structure of Ca₁.67SiHx. *Cem. Concr. Res.* **67**, 197–203 (2015).
52. Mohamed, A. K., Parker, S. C., Bowen, P. & Galmarini, S. An atomistic building block description of CSH-Towards a realistic CSH model. *Cem. Concr. Res.* **107**, 221–235 (2018).
53. Andreussi, O., Dabo, I. & Marzari, N. Revised self-consistent continuum solvation in electronic-structure calculations. *J. Chem. Phys.* **136**, 064102 (2012).
54. Manzano, H. et al. Do cement nanotubes exist? *Adv. Mater.* **24**, 3239–3245 (2012).
55. Henkelman, G., Uberuaga, B. P. & Jónsson, H. A climbing image nudged elastic band method for finding saddle points and minimum energy paths. *J. Chem. Phys.* **113**, 9901–9904 (2000).
56. Cheng, Q., Duan, J., Zhang, Q. & Jiang, L. Learning from nature: constructing integrated graphene-based artificial nacre. *ACS Nano* **9**, 2231–2234 (2015).
57. Cygan, R. T., Liang, J.-J. & Kalinichev, A. G. Molecular models of hydroxide, oxyhydroxide, and clay phases and the development of a general force field. *J. Phys. Chem. B* **108**, 1255–1266 (2004).
58. Hou, D. & Li, Z. Molecular dynamics study of water and ions transport in nano-pore of layered structure: a case study of tobermorite. *Microporous Mesoporous Mater.* **195**, 9–20 (2014).
59. Shahsavari, R., Pellenq, R. J.-M. & Ulm, F.-J. Empirical force fields for complex hydrated calcio-silicate layered materials. *Phys. Chem. Chem. Phys.* **13**, 1002–1011 (2011).
60. VandeVondele, J. et al. Quickstep: Fast and accurate density functional calculations using a mixed Gaussian and plane waves approach. *Comput. Phys. Commun.* **167**, 103–128 (2005).
61. Krack, M. Pseudopotentials for H to Kr optimized for gradient-corrected exchange-correlation functionals. *Theor. Chem. Acc.* **114**, 145–152 (2005).
62. VandeVondele, J. & Hutter, J. Gaussian basis sets for accurate calculations on molecular systems in gas and condensed phases. *J. Chem. Phys.* **127**, 114105 (2007).
63. Suk, J. W., Piner, R. D., An, J. & Ruoff, R. S. Mechanical properties of monolayer graphene oxide. *ACS Nano* **4**, 6557–6564 (2010).

Acknowledgements

The authors are grateful for the financial support of the Australian Research Council. The authors acknowledge the use of instruments and scientific and technical assistance at the Monash Centre for Electron Microscopy, a Node of Microscopy Australia. This work was performed in part at the Melbourne Centre for Nanofabrication (MCN) in the Victorian Node of the Australian National Fabrication Facility (ANFF). The authors acknowledge use of the facilities and the assistance of Ms Yvonne Hora at the Monash X-ray Platform.

Author contributions

They designed and carried out experiments, analysed the data and co-wrote the manuscript. S.C. provided guidance on theoretical model and simulation calculations. K.S. provided guidance and constructive ideas throughout the project. All authors discussed the results and commented on the manuscript. W.D. directed the entire study.

Competing interests

The authors declare no competing interests.

Additional information

Supplementary information The online version contains supplementary material available at <https://doi.org/10.1038/s43246-021-00191-6>.

Correspondence and requests for materials should be addressed to E.S. or W.D.

Peer review information *Communications Materials* thanks the anonymous reviewers for their contribution to the peer review of this work. Primary handling editor: John Plummer. Peer reviewer reports are available.

Reprints and permission information is available at <http://www.nature.com/reprints>

Publisher's note Springer Nature remains neutral with regard to jurisdictional claims in published maps and institutional affiliations.



Open Access This article is licensed under a Creative Commons Attribution 4.0 International License, which permits use, sharing, adaptation, distribution and reproduction in any medium or format, as long as you give appropriate credit to the original author(s) and the source, provide a link to the Creative Commons license, and indicate if changes were made. The images or other third party material in this article are included in the article's Creative Commons license, unless indicated otherwise in a credit line to the material. If material is not included in the article's Creative Commons license and your intended use is not permitted by statutory regulation or exceeds the permitted use, you will need to obtain permission directly from the copyright holder. To view a copy of this license, visit <http://creativecommons.org/licenses/by/4.0/>.

© The Author(s) 2021, corrected publication 2021